

Computational modeling of plasmonic thin-film terahertz photoconductive antennas

NATHAN BURFORD^{1,*} AND MAGDA EL-SHENAWEE²

¹Microelectronics-Photonics Program, University of Arkansas, Fayetteville, Arkansas 72701, USA

²Department of Electrical Engineering, University of Arkansas, Fayetteville, Arkansas 72701, USA

*Corresponding author: nburford@uark.edu

Received 6 December 2015; revised 25 January 2016; accepted 25 February 2016; posted 26 February 2016 (Doc. ID 255227); published 25 March 2016

This work presents a computational approach for investigating terahertz photoconductive antennas with enhanced performance via thin-film plasmonic electrode configurations. The commercially available finite element method solver COMSOL Multiphysics is implemented to solve Maxwell's wave equations along with the coupled drift-diffusion/Poisson's equations. The proposed approach is compared with other computational and experimental results from the literature, showing good agreement. A nanodisk array is deposited on top of a 120 nm LT-GaAs layer with the antenna electrodes located below the photoconductive layer. A femtosecond optical pump is utilized to excite the photoconductive antenna. The obtained results demonstrated significant increase in the conversion of optical energy to photocurrents as compared with conventional antennas and other plasmonic antennas from the literature. The proposed thin-film antenna with plasmonic nanostructures showed the greatest improvement in peak photocurrent—almost 336 times higher than the conventional antenna. Additionally, the thin-film antenna demonstrates a fast device response time even at a long carrier lifetime of 48 ps. The results support the capability of the proposed design to yield high optical-to-terahertz conversion efficiency, addressing the problem of low output power in terahertz photoconductive antennas. © 2016 Optical Society of America

OCIS codes: (040.2235) Far infrared or terahertz; (230.0250) Optoelectronics; (320.7080) Ultrafast devices; (250.5403) Plasmonics; (060.2370) Fiber optics sensors.

<http://dx.doi.org/10.1364/JOSAB.33.000748>

1. INTRODUCTION

Exploration into the terahertz (THz) band of the electromagnetic spectrum has experienced rapid growth over the past two decades. This began in the early 2000s, when the first THz time-domain spectroscopy and imaging systems became commercially available [1,2]. These systems utilized ultrafast photoconductive antennas (PCAs) excited by sub-picosecond optical laser pulses to achieve pulsed THz emission [3]. Since then, many other technologies for the generation and detection of THz radiation have been developed, each with their own advantages and disadvantages. Systems based on THz-PCAs have the benefits of wide and continuous bandwidth, high signal-to-noise, room temperature operation, and accurate measurement of both magnitude and phase of the signal [1–4]. Many applications based on the use of THz-PCA technology have been demonstrated, including imaging of packaged electronics and fault localization [5–8], pharmaceutical screening of polymorph and hydrate forms [9,10], margin assessment of cancerous tissue [11–14], absolute thickness measurements [15,16], material characterization [17–19], and security screening

[20–23]. A major advantage of THz technology in these applications is the nondestructive nature of the radiation, meaning that samples under test are not altered during the THz scanning process. However, one of the main drawbacks of this technology is low output power (<10 μ W), a direct result of their poor optical-to-THz conversion efficiency. This limits immediate commercialization of this technology, as many applications require higher penetration depth and/or reduced data acquisition time, which are currently limited by the available power of the THz sources.

Recently, THz-PCAs utilizing plasmonic nanostructures incorporated into the antenna electrodes have been proposed [24–30]. Some of these approaches have demonstrated orders of magnitude higher power output over conventional, non-plasmonic electrodes [26–30]. Park *et al.* experimentally demonstrated enhancement of THz emission in PCAs by incorporating nanoscale metal grating structures in the gap of the dipole antenna [24]. This demonstrated an average of 2.4 times THz power enhancement across the 0.1–1.1 THz spectral range as compared with a dipole antenna without metal

nanostructures [24]. Similar work by Jooshesh *et al.* explored variations on the shape of the plasmonic structures placed in the dipole gap [25]. Utilizing periodic hexagonal structures improved the peak emitted THz photocurrent 2.9 times as compared with the previously proposed grating structures [25]. The work of Berry *et al.* has investigated several configurations of plasmonic-enhanced THz emitters [26–28]. The current best conversion efficiency by a single emitter THz-PCA was achieved by Yang *et al.* [29]. Here, 3D columns of plasmonic electrodes were fabricated to effectively increase the surface area of the LT-GaAs/metal interface while still allowing light penetration into the active layer. This configuration yielded a record high 7.5% conversion efficiency [29].

Early numerical modeling of THz generation in GaAs-based PCAs was established by Jepsen *et al.*, where the time-dependent current density inside the GaAs was described by a modified 1D Drude–Lorentz model and used to estimate the profile of the emitted THz pulse [3]. It was demonstrated that this model can effectively describe the relative dependence of the amplitude and shape of the photocurrent on the material parameters as well as operational conditions such as optical pump power, pulse shape, and bias voltage. However, this analytical method does not take into consideration the geometry-dependent radiative behavior of the dipole antenna. Several works have since addressed this issue [31–35]. Khiabani *et al.* developed an equivalent circuit model that incorporates the radiation efficiency of the THz antenna. Quantitative agreement between the predicted and measured optical-to-THz conversion efficiency was observed [31,32]. Moreno *et al.* utilized an FDTD numerical method to solve the electronic drift-diffusion/Poisson's equations in a THz-PCA. By approximating the optical pulse excitation to have a Gaussian lateral distribution and Beer–Lambert absorption profile inside the photoconductor, the time-dependent potential and carrier concentrations in the full 3D domain of the THz-PCA was calculated [33–35]. Although existing numerical methods prove effective at predicting the performance of THz-PCAs, it is important to note that all of them implement a simplified approximation of the optical field distribution inside the photoconductive region. While this is accurate for conventional style PCAs, the optical field inside a plasmonic-enhanced device is highly nonuniform and cannot be described by simplified analytical expressions.

The goal of this work is to introduce and computationally study a novel THz-PCA design with enhanced optical-to-THz conversion efficiency. Utilizing the commercially available finite element method (FEM) solver COMSOL Multiphysics, plasmonic-enhanced THz-PCAs will be studied through the combination of Maxwell's wave equation for the optical interaction and the combined Poisson's/drift-diffusion equations for the electrical response. Incorporation of the numerical solution of Maxwell's wave equation everywhere in the antenna device allows the nonuniform optical field and, consequently, the nonuniform carrier generation rate to be more accurately described.

The paper is organized as follows: Section 2 introduces the theory and concept behind the proposed THz-PCA design as well as defines the computational domain and methodology. Section 3 presents the validation of the model with both

computational and experimental work from the literature. Section 4 compares the results of the proposed THz-PCA design with other designs that have been studied in the literature. Section 5 summarizes and concludes the work.

2. THEORY

Generation of pulsed broadband THz radiation from PCAs occurs through the conversion of a sub-picosecond optical pulse to a transient current inside a photoconductive antenna. The conventional layout consists of a metallic dipole antenna, designed to operate in the THz band, biased with a DC voltage and located on top of a photoconductive substrate. In order to achieve a THz response, the time-profile of the induced photocurrent must follow (approximately) the profile of the incident femtosecond optical pulse. If the photoconductor has a carrier lifetime much greater than the optical pulse duration, the excited carriers will continue to contribute to a transient photocurrent well after the initial optical excitation. This will broaden the optically induced current pulse in the photoconductor and reduce the THz power of the emitted signal. Photoconductors with sub-picosecond carrier lifetimes such as low temperature grown gallium arsenide (LT-GaAs) allow for the necessary ultrafast response required to achieve THz operation.

A. Plasmonic Enhanced Thin-Film Photoconductive Antennas

In order to overcome low optical-to-THz conversion efficiency of conventional THz-PCAs, we propose a new plasmonic enhanced thin-film design. Thin-film photovoltaics have been proposed and extensively demonstrated for use in solar cell technology [36–39]. In such applications, high-quality active and sacrificial layers a few hundred nanometers in thickness are epitaxially grown [40]. The active layers can then be “peeled” off through a process called “epitaxial lift off,” allowing a single substrate to be reused and yield multiple high-quality solar cells [40]. In solar cells, however, this leads to lower device performance compared with their thick substrate based counterparts [36,37]. Much of the incident light is reflected out or passed through the photovoltaic thin film before being absorbed. To overcome this, the addition of plasmonic metal nanostructures on the thin-film surface has been proposed to concentrate the incident optical energy in the near-field of the nanostructures. This increases the total photon density in the photoconductive layer, consequently improving the photocarrier generation rate [38,39].

We propose a new plasmonic thin-film THz-PCA design, which utilizes the characteristics of thin-film solar cells to offer improved optical-to-THz conversion efficiency. The device geometry is illustrated in Fig. 1. Figure 1(a) shows a 3D view of the THz-PCA chip mounted on high-resistivity silicon (Si) lens. The LT-GaAs layer is rendered as semitransparent to allow the location of the antenna anode and cathode to be easily observed. The infrared optical pump is incident from the $-z$ direction and focused over the antenna anode. Photocarriers generated in the LT-GaAs contribute to a driving current for the antenna, producing THz radiation, which is coupled out of the device by the Si lens. A top view of the x - y plane is shown in Fig. 1(b). The location of the antenna

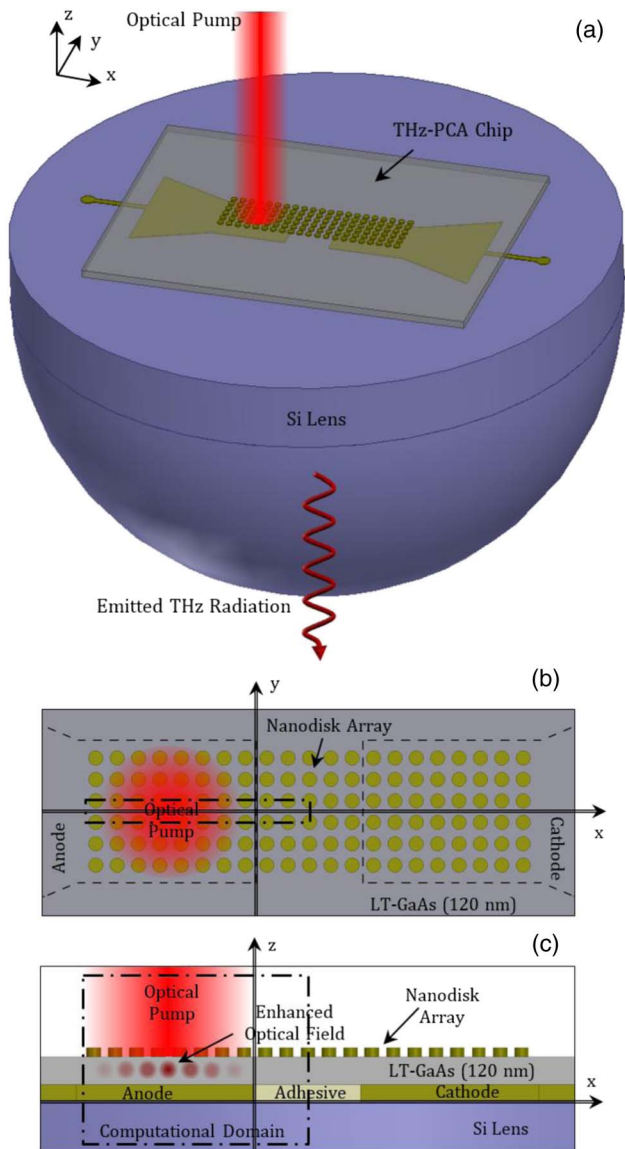


Fig. 1. Illustration of the proposed plasmonic thin-film THz-PCA design (dimensions not to scale to show details). (a) 3D isometric view of the THz-PCA mounted on a Si THz lens. (b) x - y , plane top view of the device, antenna electrode locations outlined by the dashed black lines. (c) x - z , plane cross-section view, nanodisk array located on top of the 120 nm thick LT-GaAs photoconductive layer; THz-PCA anode and cathode located on the bottom of the LT-GaAs. Device is mounted with adhesive to the Si lens for mechanical support as well as coupling of the THz radiation out of the device. Computational domain is indicated in (b) and (c) by the dot-dashed outline.

anode and cathode is illustrated by the dashed black line, as these are located under the LT-GaAs layer. A gold (Au) nanodisk array covers the top of the LT-GaAs across the relative location of the antenna anode, gap, and cathode. The nanodisk array is included over all regions to allow future investigation of plasmonic-enhanced optical excitation of regions other than the anode. Additionally, fabrication of the actual device would be simplified by roughly aligning a large nanodisk array over the entire region rather than fine alignment to ensure the array is

only over the anode. Figure 1(c) shows an x - z cross section of the device taken at the y coordinate corresponding to the device center. The computational domain to be considered in this work is outlined in Figs. 1(b) and 1(c) by the dotted-dashed outline. The THz-PCA anode and cathode are located on the bottom of the LT-GaAs thin-film layer, while an array of plasmonic nanodisks is located on the top surface. In the gap separating the anode and cathode, there is a dielectric adhesive layer because, during fabrication, such a layer will be necessary to attach the device to the Si lens. The incident optical pump excites plasmon resonances in the nanodisk array, leading to the enhanced optical field in the LT-GaAs layer. In addition to the plasmonic enhancement, the proposed thin-film PCA will have improved performance due to complete usage of the available optical pump area. In LT-GaAs, only the carriers generated within around 100 nm from the anode will be collected. The carriers generated further away will recombine due to the sub-picosecond carrier lifetime of the material. Therefore, in a conventional PCA, where the optimal location of the optical pump is centered on the anode edge [41], the generated carriers will be much less than those generated in the proposed thin-film PCA, where the optical pump is centered over the anode, as shown in Fig. 1.

B. Computational Domain

Due to the fine meshing requirements needed to accurately solve the near field of plasmonic nanostructures [38,39,42], several approximations are made to reduce the computational domain, as shown in Figs. 1(b) and 1(c).

1. Considering only the interaction between the optically induced photocurrent and the electrode induced DC bias in the LT-GaAs, the antenna radiating element, microstrip lines, and bias pads are neglected.
2. Asymmetric optical excitation focused on the anode, as shown in Fig. 1(b), allows the domain to be reduced by half at the center of the gap.
3. Geometric periodicity allows plasmonic electrode structures with periodicity along the y direction to be modeled while greatly reducing the computational complexity, as shown in Fig. 1(b).

These approximations allow the computational domain to be reduced to a point where nanoscale structuring of the electrodes can be modeled with sufficiently fine meshing with reasonable computational resources. To illustrate this, consider that some of the configurations to be discussed in this work require approximately 500,000 mesh elements in the photoconductor region to ensure numerical accuracy. Without implementing approximation 2 and 3, the number of mesh cells needed to produce the same level of refinement would be at least 50 times larger, on the order of 25 million mesh elements.

C. FEM Modeling of Pulsed THz Generation in PCAs

Computational modeling was divided into two steps, (1) the optical response found by calculation of the spatial distribution of the optical field using the frequency-domain form of the electromagnetic wave equation; (2) the electronic response found by solving the time-domain forms of the coupled

drift-diffusion and Poisson's equations under carrier generation derived from the optical field from the first step. By implementing several approximations to decouple the optical and electrical responses, the model complexity was reduced while still accounting for the primary factors determining the induced THz photocurrent response.

1. Optical Response

The optical response was determined by solving the electromagnetic wave in Eq. (1) in the frequency domain:

$$\nabla \times \mu_r^{-1} (\nabla \times \vec{E}) - k_o^2 \left(\epsilon_r - \frac{j\lambda\sigma}{2\pi c\epsilon_o} \right) \vec{E} = 0. \quad (1)$$

Here, ϵ_r , σ and μ_r are the relative electrical permittivity, electrical conductivity and magnetic permeability for the material, k_o and ϵ_o are the free-space propagation constant and permittivity, λ is the wave excitation wavelength, c is the speed of light in vacuum, and \vec{E} is the complex electric field vector. The optical excitation field was defined to have Gaussian dependence along the x axis according to

$$\vec{E}_{\text{inc}} = \hat{a}_e E_o \exp \left(2 \ln(0.5) \frac{(x - x_o)^2}{D_x^2} \right), \quad (2)$$

with \hat{a}_e being the polarization unit vector, x_o being the center location of the Gaussian beam, and D_x being the half-power beam width (HPBW) along the x axis. The electric field amplitude, E_o , corresponds to the peak electric field, spatially and temporally, of the femtosecond pulse optical excitation and can be approximated by Eq. (3):

$$E_o = \sqrt{\frac{P_{\text{ave}} 8\eta_o}{f_p D_x D_y D_t}} \left(-\frac{\ln(0.5)}{\pi} \right)^{3/4}. \quad (3)$$

P_{ave} , f_p , and D_t are the average laser power, pulse repetition rate, and pulse time duration, respectively, and are common defining parameters of femtosecond pulse laser sources. η_o is the free-space wave impedance. Although the excitation in this model has Gaussian dependence in the x direction only, the real optical beam is Gaussian in the y direction as well, with a HPBW of D_y . When modeling a real experimental configuration, D_y must be taken into account in order to calculate the correct peak electric field through Eq. (3).

Upon solving Eq. (1), the optical field distribution \vec{E} was found everywhere in the computational domain. From here, the vector components of the power flux density can be calculated from Eqs. (4)–(6), where $\hat{\eta}$ is the material dependent complex wave impedance:

$$P_{ox}(x, y, z) = \frac{1}{2\hat{\eta}} \text{Re}(|E_y|^2 - |E_z|^2), \quad (4)$$

$$P_{oy}(x, y, z) = \frac{1}{2\hat{\eta}} \text{Re}(|E_z|^2 - |E_x|^2), \quad (5)$$

$$P_{oz}(x, y, z) = \frac{1}{2\hat{\eta}} \text{Re}(|E_x|^2 - |E_y|^2). \quad (6)$$

The total power flux density in units of W/m² is

$$P_s(x, y, z) = (|P_{ox}(x, y, z)|^2 + |P_{oy}(x, y, z)|^2 + |P_{oz}(x, y, z)|^2). \quad (7)$$

In order to derive an expression for the carrier generation rate inside of the photoconductor, an approximation was made that each photon with energy $E_p > E_g$ (where E_g is the semiconductor bandgap energy) absorbed in the photoconductor generates a single electron-hole pair [43]. The time-dependent carrier generation rate was approximated by [43]

$$g(x, y, z, t) = (4\pi k_{\text{PC}}/hc) P_s(x, y, z) \exp \left(4 \ln(0.5) \frac{(t - t_o)^2}{D_t^2} \right), \quad (8)$$

where k_{PC} is the imaginary part of the refractive index for the photoconductor, h is Planck's constant, c is the speed of light in vacuum, t_o is the pulse center time, and D_t is the pulse FWHM. Equation (8) gives both the spatial and temporal carrier generation, in units of s⁻¹ m⁻³ inside the photoconductive region.

The boundary conditions for the optical response are periodic on the x - z boundaries and absorbing impedance-matched boundaries are assumed on all other faces. The excitation was incident in the $-z$ direction, with polarization and center location varying depending on the configuration of the electrodes under consideration. The various model parameters utilized in Eqs. (1)–(8) vary throughout the different studies of this work. Therefore, tables will be included to summarize the values used in each case.

2. Electrical Response

With the optically induced carrier generation derived from the optical response analysis, the time-dependent carrier dynamics can be solved. The model utilized for this step was the standard, time-domain form of the coupled Poisson's in Eq. (9) and drift-diffusion in Eqs. (10) and (11):

$$\epsilon_o \nabla \cdot (\epsilon_r \nabla V) = q(n - p - N_D + N_A), \quad (9)$$

$$\frac{\partial n}{\partial t} = -\frac{1}{q} \nabla \cdot \left\{ -\mu_n q \nabla (V + \chi) n + \mu_n k_B T G \left(\frac{n}{N_c} \right) \nabla n \right\} - r(x, y, z) + g(x, y, z, t), \quad (10)$$

$$\frac{\partial p}{\partial t} = \frac{1}{q} \nabla \cdot \left\{ -\mu_p q \nabla (V + \chi + E_g) p + \mu_p k_B T G \left(\frac{p}{N_v} \right) \nabla p \right\} - r(x, y, z) + g(x, y, z, t). \quad (11)$$

The unknowns in this system of equations are V , n and p , the electric potential, electron concentration, and hole concentration, respectively. q is the electron charge, ϵ_o is the permittivity of free space, and k_B is the Boltzmann constant. For clarity, all other quantities are defined in Table 1, with associated nominal values used in this work to model LT-GaAs. As demonstrated by Moreno *et al.* [33], the inclusion of field-dependent carrier mobility has a significant impact on the outcome of numerical modeling of THz-PCAs through the drift-diffusion equations. To account for this, the empirical Caughey–Thomas model was utilized to modify the electron and hole mobility, μ_n and μ_p at varied electric fields [44]. Carrier recombination was described by the Schottky–Read–Hall and Auger recombination models [43]:

Table 1. Electrical Properties and Constants of Eqs. (9)–(12)

Symbol	Description	Units	Value
ϵ_r	LT-GaAs	None	13.3
N_D	Donor doping concentration	$1/\text{cm}^3$	$1 \cdot 10^{15}$
N_A	Acceptor doping concentration	$1/\text{cm}^3$	0
μ_n	Low-field electron mobility	$\text{m}^2/\text{V}/\text{s}$	0.8
μ_p	Low-field hole mobility	$\text{m}^2/\text{V}/\text{s}$	0.047
E_g	Bandgap	V	1.424
χ	Electron affinity	V	4.07
T	Room temperature	K	300
N_c	Conduction band density of states	$1/\text{m}^3$	$2.18 \cdot 10^{-23}$
N_v	Valence band density of states	$1/\text{m}^3$	$5.43 \cdot 10^{-24}$
τ_n	SRH electron lifetime	s	$480 \cdot 10^{-12}$
τ_p	SRH hole lifetime	s	$480 \cdot 10^{-12}$
γ_n	Electron degeneracy factor	None	2
γ_p	Hole degeneracy factor	None	4
C_n	Auger electron coefficient	cm^6/s	$7 \cdot 10^{-30}$
C_p	Auger hole coefficient	cm^6/s	$7 \cdot 10^{-30}$
$n_{i,\text{eff}}$	Effective intrinsic carrier concentration	$1/\text{m}^3$	$1.23 \cdot 10^{-12}$

$$r(x, y, z) = \frac{np - \gamma_n \gamma_p n_{i,\text{eff}}^2}{\tau_p(n + \gamma_n n_{i,\text{eff}}) + \tau_n(p + \gamma_p n_{i,\text{eff}})} + (C_n n + C_p p)(np - \gamma_n \gamma_p n_{i,\text{eff}}^2). \quad (12)$$

It is important to note that, for the electrical response, only the LT-GaAs layer was considered. The boundary conditions are periodic on the x - z faces, ohmic contact boundaries at the anode and gap-centered y - z face with fixed bias voltages $V = V_{\text{bias}}$ and $V_{\text{bias}}/2$, respectively. All other faces are electrical insulation boundaries.

3. Approximations

It is important to consider the approximations used in this model. The optical pulse is time-dependent and non-monochromatic. As such, the variation of the wavelength-dependent material properties should be considered in order to provide a complete description. However, the bandwidth of the femtosecond pulse is relatively narrow, $\Delta\lambda = 9.4$ nm for a pulse with center frequency $\lambda = 800$ nm and width of $D_t = 100$ fs. Of all the materials considered in this model, the highest variance across this bandwidth range occurs in the conductivity of Au up to 3.28%. Although the error this approximation introduces may not be significant here, it is important to note that wider bandwidth pulses will introduce increased variance in the material optical properties.

A second effect arising from the conductivity time-dependence on the optically induced carrier concentration is neglected in this model. This is the carrier screening effect, where excited carriers in the photoconductor will contribute to an increase in the effective optical conductivity. The effect manifests as an increase in surface reflectivity as the pulse propagates into the photoconductor and excites additional carriers. This approximation has led the proposed model to utilize

underestimated conductivity leading to overestimation of the induced photocurrent.

The above approximations resulted from the iterations between the optical and electrical computational domains at each time step. Currently, solving the optical domain a single time requires approximately 43 min on a dual Intel six-core Xeon X5670 2.93 GHz processor system, in addition to around 1.5 h to complete the time-stepping in the electrical domain. Inclusion of the carrier screening effect (i.e., the increase in conductivity with time) would require the optical domain to be solved at each of the 200 or more iterations of the time-stepping process currently used in the model.

3. MODEL VALIDATION

In order to demonstrate the validity of the proposed model, comparison against both computational and experimental work from the literature was performed here. For comparison of this work to other models, consider the computational work established by Moreno *et al.* [34], where the FDTD method and a similar set of coupled Poisson's/drift-diffusion equations was utilized. The method in [34] did not utilize any of the domain reduction approximations proposed here, thereby providing a more complete analysis of the electro-optical interaction in conventional THz-PCAs. Another distinct difference was that the model in [34] did not calculate the spatially dependent optical field through the solving of Maxwell's equations. Rather, Moreno *et al.*'s method approximates the optical field with an analytical Gaussian dependence in the lateral direction and a Beer-Lambert's dependence in the depth of the photoconductor. Described in [34] was a face-to-face dipole antenna with a 5 μm gap, located on LT-GaAs. The transient photocurrent was calculated at the center of the gap (see Fig. 8 in [34]). Similarly, using the proposed method here, the photocurrent at the gap center is calculated in a conventional THz-PCA geometry of the same dimensions as the face-to-face dipole described in [34]. Table 2 summarizes the model parameters use in this study for Eqs. (1)–(8). Note that the value of $P_{\text{ave}} = 3.57$ mW is higher than that reported in [34]. This accounts for the air/LT-GaAs reflection losses in our model, which are not considered in [34]. It is important to note that the Gaussian beam formulation of this work appears different than that used in [34]. However, the Gaussian dependence in both x and t is numerically identical in both works.

Comparison of the results from Moreno *et al.* to calculations utilizing the model proposed in this work is illustrated in Fig. 2(a). The solid line is the photocurrent calculated using the proposed model at a point located at the center of the gap and surface of the photoconductor, and the **X** marks represent the corresponding results taken from [34]. The optical excitation is temporally centered at $t_0 = 3$ ps in both cases. Both results are normalized to the peak value of 0.02 A/ μm^2 reported in [34]. The results from this work have a peak value of 0.0126 A/ μm^2 occurring at 3.09 ps and an FWHM of 0.42 ps. In comparison, the reference results of Moreno *et al.* have a peak value of 0.02 A/ μm^2 occurring at 3.12 ps and a FWHM of 0.63 ps.

The general trend observed in both models agrees, but the peak amplitude of the current model is almost 58% of the peak in [34]. There are notable differences in the two methods. This

Table 2. Optical Properties and Constants of Eqs. (1)–(8) for Validation Study with Moreno *et al.* [34]

Symbol	Description	Units	Value
λ	Free-space wavelength	nm	780
P_{ave}	Average laser power	mW	3.57
f_p	Laser pulse repetition rate	MHz	80
x_o	Pulse x -axis center location	μm	2.5
t_o	Pulse center location (time)	ps	3
D_x	Pulse HPBW (x direction)	μm	3
D_y	Pulse HPBW (y direction)	μm	3
D_t	Pulse FWHM (time)	fs	133
V_{bias}	DC bias voltage	V	30
ϵ_r	Ti [48]	None	-6.61
ϵ_r	Au [49]	None	-22.5
ϵ_r	LT-GaAs [47]	None	13.7
σ	Ti [48]	S/m	$42 \cdot 10^3$
σ	Au [49]	S/m	$2.4 \cdot 10^3$
σ	LT-GaAs [47]	S/m	$1.1 \cdot 10^3$
μ_r	Magnetic permeability (all regions)	None	1
k_{PC}	Photoconductor extinction coefficient of LT-GaAs [47]	None	0.0625
\hat{a}_e	\vec{E}_{inc} polarization unit vector	None	\hat{a}_x

difference is mainly due to the approximation of the wave equation solution. In this work, the wave equation is solved using the computational FEM method, while in [34] the wave equation was approximated using the Beer–Lambert’s equation. A comparison of the power density inside the LT-GaAs at the center of the gap is shown in Fig. 2(b), demonstrating almost a 53% difference between the two methods. The difference in the power density nearly matches the difference in the peak photocurrent in Fig. 2(a). In addition, for the carrier mobility model, we used the Caughey–Thomas equation as a function of the local electric potential [44]. The work of Moreno *et al.* used the MINIMOS set of equations where the effects of lattice, impurity, and surface carrier scattering were included [45]. These differences in the carrier mobility model as well as the differences in the Beer–Lambert’s approximation in [34] and the full wave solution of the optical field in our model are the main contributors leading to a lower photocurrent and optical power density observed in this work as compared with [34].

Another validation is presented here with the plasmonic enhancement of the photocurrent, which has been experimentally observed in the work of Berry *et al.* [26]. The two electrode configurations are a conventional, non-plasmonic electrode and the plasmonic electrodes with a nanoscale grating geometry. We basically modeled the exact configurations in [26] and compared the numerical results with their experimental data. The time-averaged photocurrent collected by the antenna was calculated for both configurations as a function of incident optical power, P_{ave} . Table 3 summarizes the model parameters use in this study for Eqs. (1)–(8).

Comparison of the current model to experimentally observed reference results in [26] is illustrated in Fig. 3. This shows the photocurrent enhancement, defined as the ratio of time-averaged photocurrents of the plasmonic and conventional antennas, as a function of incident optical power.

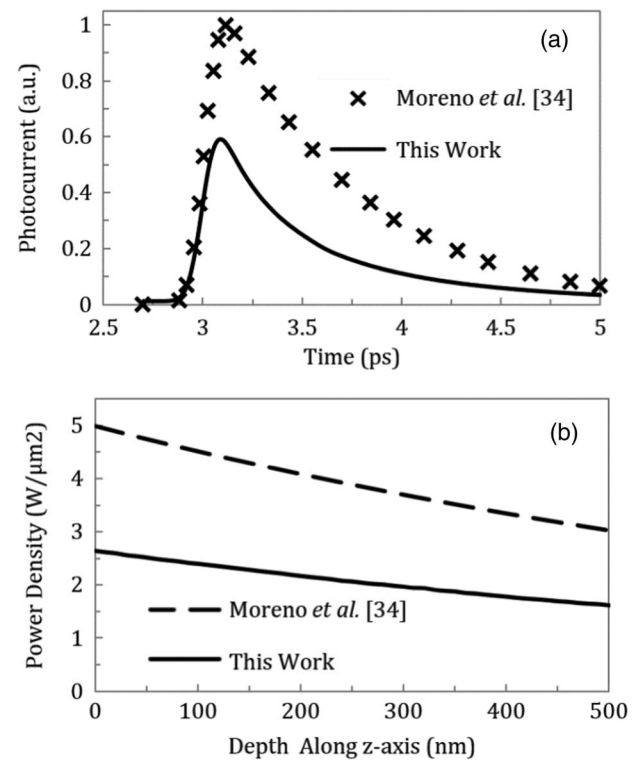


Fig. 2. (a) Comparison of the calculated photocurrent at the center of the gap. Solid trace represents the results found using this model; X marks are points traced from Fig. 8 in Moreno *et al.* [34]. (b) Optical power density at the center of the gap versus depth inside the LT-GaAs. Dashed line represents the Beer–Lambert’s approximation utilized in [34]; solid line represents this work, the full-wave solution of Maxwell’s equation.

Table 3. Optical Properties and Constants of Eqs. (1)–(8) for Validation Study with Berry *et al.* [26]

Symbol	Description	Units	Value
λ	Free-space wavelength	nm	800
P_{ave}	Average laser power	mW	0.5–25
f_p	Laser pulse repetition rate	MHz	76
x_o	(conventional)	μm	0
x_o	(nanograting)	μm	-2.5
t_o	Pulse center location (time)	ps	0
D_x	Pulse HPBW (x direction)	μm	5
D_y	Pulse HPBW (y direction)	μm	5
D_t	Pulse FWHM (time)	fs	200
V_{bias}	DC bias voltage	V	40
ϵ_r	Ti [48]	None	-6.21
ϵ_r	Au [49]	None	-24.1
ϵ_r	LT-GaAs [47]	None	13.6
σ	Ti [48]	S/m	$42 \cdot 10^3$
σ	Au [49]	S/m	$2.5 \cdot 10^3$
σ	LT-GaAs [48]	S/m	$1.0 \cdot 10^3$
μ_r	Magnetic permeability (all regions)	None	1
k_{PC}	Photoconductor extinction coefficient of LT-GaAs [47]	1/cm	0.086
\hat{a}_e	(conventional)	None	\hat{a}_x
\hat{a}_e	(nanograting)	None	\hat{a}_y

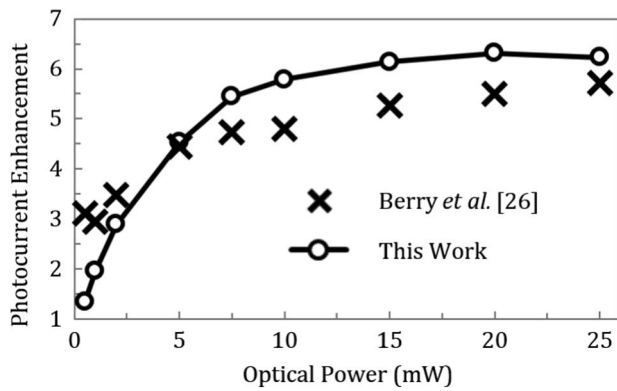


Fig. 3. Comparison of the calculated photocurrent enhancement to experimental values reported by Berry *et al.* [26]. Solid line with circle marks represent calculated results using this model; X marks represent the reference results calculated from the inset data of Fig. 3(b) in the work of Berry *et al.* [26].

The X marks represent the reference results calculated from the inset data of Fig. 3(b) in the work of Berry *et al.* [26]. The open circles are the results calculated using the model here. In general, there is good agreement in the trend and in the magnitude of the photocurrent enhancement. At $P_{\text{ave}} = 5$ mW, the difference between the reference and calculation was minimal at less than 2%. In conclusion, the current model demonstrates good agreement with the experimental work of [26]. For optical powers greater than 5 mW, the model slightly overestimates the photocurrent enhancement. Local heating has been observed in THz-PCAs under high optical pump power, which can reduce the quantum efficiency of the device [25]. The model assumes a constant 300K temperature and currently does not account for this phenomenon, which could explain the difference between the current model and experiment in [26].

4. NUMERICAL RESULTS

With the computational methodology validated against theoretical and experimental examples from the literature, the next step is to analyze the THz-PCA electrodes with new geometric configurations. As previously discussed, the main cause of the low optical-to-THz power conversion in PCAs comes from short (< 1 ps) carrier lifetime necessary to achieve ultrafast operation. This is illustrated in Fig. 4, which shows computational results of the transient electrode current in a conventional PCA with a 0.48 ps carrier lifetime (solid line) and 48 ps carrier lifetime (dashed line). Here, it is noted that the 0.48 ps carrier lifetime allows for the transient current to more closely follow the profile of the excitation, resulting in a narrower pulse and better THz performance as compared with the 48 ps carrier lifetime case.

To overcome this, we propose the new bottom-located thin-film (BLTF) and plasmonic bottom-located thin-film (P-BLTF) THz-PCA geometries, as illustrated in Figs. 5(a) and 5(b), respectively. In addition to these new electrode designs, top-located plasmonic nanograting electrode and conventional electrode designs are considered for comparison, as shown in Figs. 5(c) and 5(d). The plasmonic nanograting design has been

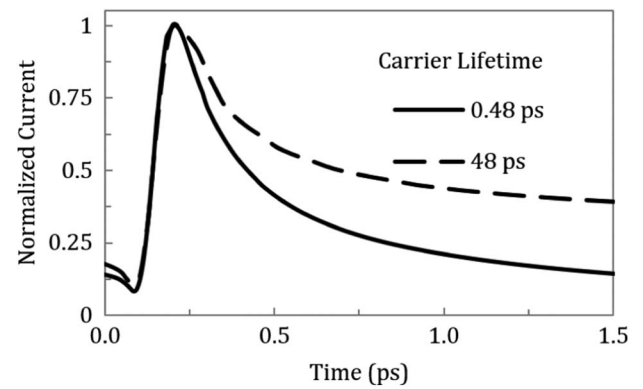


Fig. 4. Anode current versus time for a conventional style THz-PCA shown in Fig. 5(d) under 100 fs pulsed optical excitation. Carrier lifetime varied from 0.48 ps (solid line) to 48 ps (dashed line).

previously studied by several groups [26–30,46], and, for this work, the geometry proposed by Berry *et al.* will be utilized [26]. The THz performance can be compared between designs by considering two characteristics of the induced current pulse: the peak value of the current and the pulse FWHM. As a first approximation, higher peak current indicates higher total THz power, while a low FWHM will give a wider THz bandwidth.

For all four antenna designs, the gap between the anode and cathode was 20 μm , and a 0.5 μm air layer was included above the photoconductor. For the conventional and nanograting, the LT-GaAs layer has a 0.5 μm depth. For the BLTF and P-BLTF designs, a 0.5 μm dielectric substrate layer was included under the antenna and LT-GaAs. The dimensions of the BLTF and P-BLTF electrodes are determined by parametric optimization of the geometry in order to maximize the average electric field inside the LT-GaAs layer at an 800 nm wavelength and 1 V/m optical excitation. For both these designs, the thickness of the thin-film LT-GaAs layer is set to 120 nm. For the P-BLTF design, the nanodisk structures are set to a diameter of 200 nm, center-to-center spacing of 520 nm and a total height of 75 nm. The nanodisks are comprised of a 5 nm Ti adhesion layer, followed by a 70 nm Au layer. The frequency-dependent optical properties ϵ_r and σ are taken from Aspnes *et al.* for GaAs [47], Johnson and Christy for Ti [48] and Rakić *et al.* for Au [49]. Table 4 summarizes the values of the model parameters used in this study for Eqs. (1)–(8).

The plasmonic behavior of the nanodisks is illustrated in Fig. 6. In Fig. 6(a), the average electric field inside the LT-GaAs layer is calculated as a function of excitation wavelength for two proposed designs. For the P-BLTF design, a peak in the average electric field was observed at 800 nm. This is characteristic of a plasmonic resonance in the nanostructures efficiently coupling the incident electromagnetic energy into the LT-GaAs thin-film layer. At the 800 nm excitation wavelength, the average electric field is 0.70 and 0.35 V/m for the P-BLTF and BLTF designs, respectively. This indicates a two times increase in the average optical field due to the addition of the plasmonic nanostructures. In addition to the LT-GaAs absorption spectra, the power reflectance spectra for the BLTF and P-BLTF designs are shown in Fig. 6(b). Power reflectance is

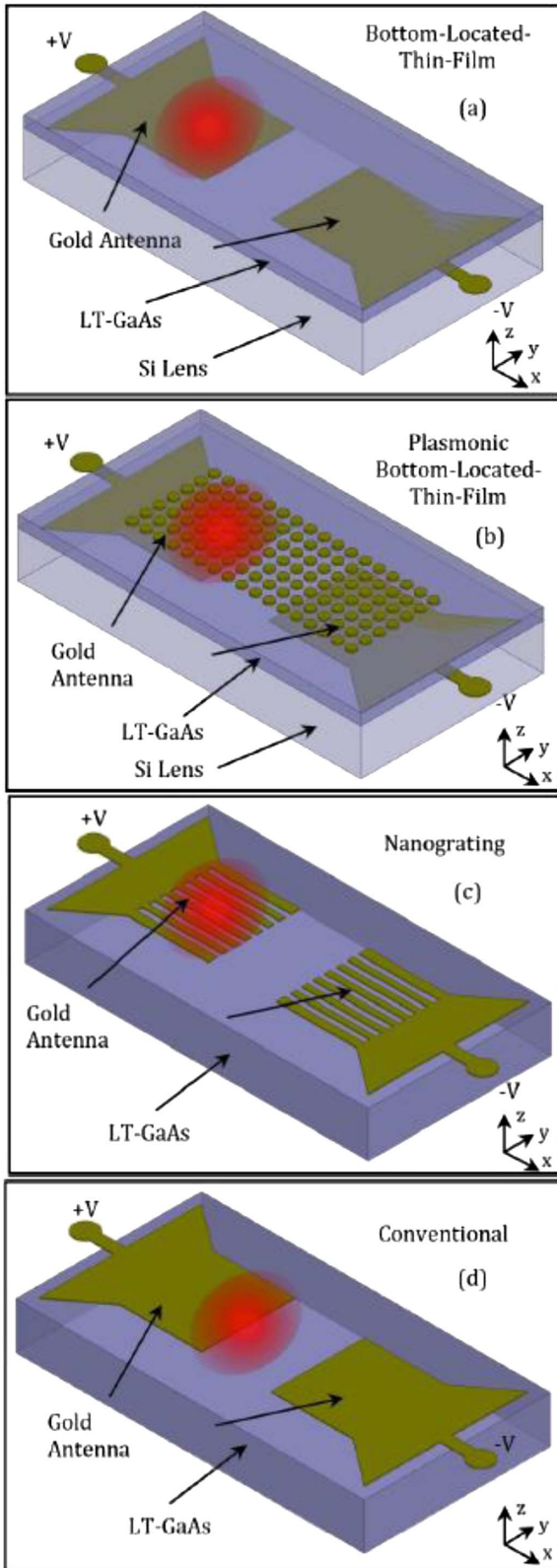


Fig. 5. Illustrations of the various THz-PCA electrode designs considered in this work. (a) Bottom-located thin film. (b) Plasmonic bottom-located thin film. (c) Plasmonic nanograting top-located electrodes [26]. (d) Conventional top-located electrodes.

Table 4. Optical Properties and Constants of Eqs. (1)–(8) for Comparison Study of the BLTF, P-BLTF, Nanograting, and Conventional PCA Designs

Symbol	Description	Units	Value
λ	Free-space wavelength	nm	800
P_{ave}	Average laser power	mW	10
f_p	Laser pulse repetition rate	MHz	76
x_o	(conventional)	μm	0
x_o	(BLTF, P-BLTF, and nanograting)	μm	-2.5
t_o	Pulse center location (time)	ps	0
D_x	Pulse HPBW (x direction)	μm	5
D_y	Pulse HPBW (y direction)	μm	5
D_t	Pulse FWHM (time)	fs	100
V_{bias}	DC bias voltage	V	40
ϵ_r	Ti [48]	None	-6.21
ϵ_r	Au [49]	None	-24.1
ϵ_r	LT-GaAs [47]	None	13.6
σ	Ti [48]	S/m	$42 \cdot 10^3$
σ	Au [49]	S/m	$2.5 \cdot 10^3$
σ	LT-GaAs [48]	S/m	$1.0 \cdot 10^3$
μ_r	Magnetic permeability (all regions)	None	1
k_{PC}	Photoconductor extinction coefficient of LT-GaAs [47]	1/cm	0.086
\hat{a}_e	(conventional)	None	\hat{a}_x
\hat{a}_e	(BLTF, P-BLTF and nanograting)	None	\hat{a}_y

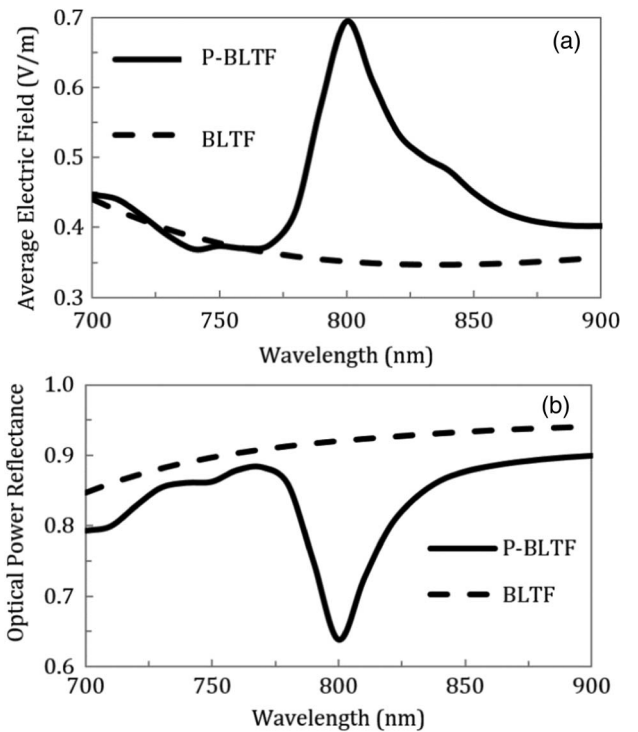


Fig. 6. (a) Average electric field absorbed in the LT-GaAs layer under 1 V/m optical excitation as a function of excitation wavelength. (b) Optical power reflectance spectrum. Dashed line represents the BLTF design; solid line represents the P-BLTF design.

found by calculating the average z component of the Poynting vector at the top x - y boundary of the computational domain and dividing it by the average incident optical power. For the P-BLTF, the peak in the plasmonic resonance is observed at 800 nm. Interesting to note is that, in the reflection spectrum for the P-BLTF and BLTF, the minimum reflectance observed at 800 nm is 64% and 92%, respectively.

The numerical accuracy of the new models is assured by testing the convergence of the model for the increasing total number of mesh elements. The results of this study are illustrated in Fig. 7. Here, the current at the anode was calculated versus time in the P-BLTF model for different numbers of mesh elements (inside the semiconductor region), ranging from 6k to 426k. The inset illustrates the relative error with an increasing number of elements, calculated from the peak value of the photocurrent. Here, it is observed that, at 118k mesh cells, the relative error was below 5%, and the minimum observed relative error was 1.5% at 426k mesh cells. Therefore, to keep the numerical error minimized, the meshing parameters, which yielded 426k for this geometry, are applied to all other geometries described in this work.

The time-dependent photocurrent of each of the four anode geometries is calculated under similar conditions to study each design's ability to convert the incident optical pulse to a collectable photocurrent. The results are shown in Fig. 8, which covers a range greater than four orders of magnitude. The conventional anode design has the lowest overall photocurrent response, followed by the nanograting, BLTF, and finally P-BLTF design, which has the strongest response. Peak photocurrent of each design is 0.17, 1.7, 14.8, and 56.8 mA for the conventional, nanograting, BLTF, and P-BLTF designs, respectively. In addition to peak photocurrent, the FWHM of the current pulse is another performance factor to consider because smaller FWHM translates to increased power at higher THz frequencies. The FWHM is found from the data in Fig. 8 by measuring the time span between the half-maximum values for each curve and is 170, 221, 258, and 280 fs for the BLTF, P-BLTF, conventional, and nanograting designs, respectively.

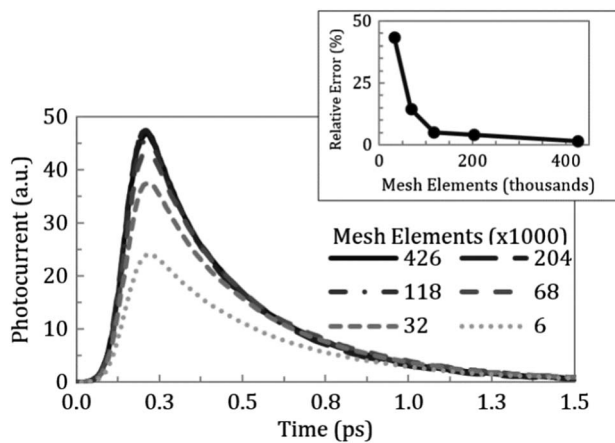


Fig. 7. Photocurrent collected at the anode for the P-BLTF design for varying number of mesh elements in the photoconductive layer. Inset illustrates the relative error with increasing number of mesh elements.

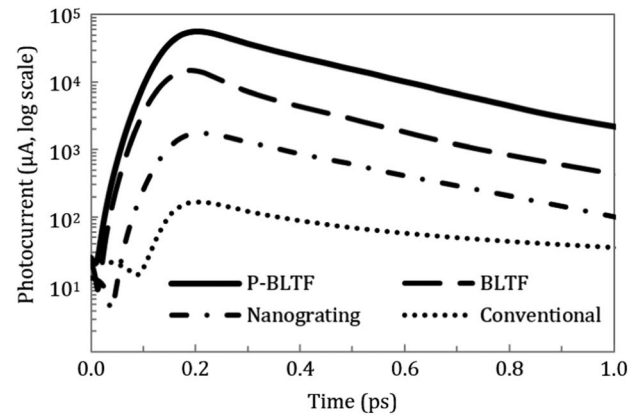


Fig. 8. Anode photocurrent response versus time for each of the four THz-PCA electrode designs.

Numerical methods currently exist that allow the output power of a THz-PCA to be calculated, once the optically induced photocurrent is known [3,31–35]. However, in [26] it has been reported that regardless of electrode design and incident optical power, the output THz power is linearly proportional to the photocurrent. The results in Fig. 8 show that the peak photocurrent enhancement for the P-BLTF as compared with conventional design is approximately 300. Therefore, the expected output THz power of the P-BLTF could be 300 times larger than the output power of a conventional emitter. Because conventional emitters generally have optical-to-THz conversion efficiencies on the order of 10^{-5} – 10^{-4} , the P-BLTF design would provide output power of ~ 30 – 300 μ W versus the conventional emitter that would provide ~ 0.1 – 1 μ W.

To illustrate the mechanism leading to the increased BLTF and P-BLTF designs, the peak electric field was plotted in the x - z cross-section plane of the domain for both P-BLTF and BLTF designs, as shown in Figs. 9 and 10, respectively. Here, it was observed that the maximum optical field is up to two times higher in the region inside the LT-GaAs in between adjacent nanodisks. This leads to the higher peak photocurrent observed in the P-BLTF design. The higher FWHM observed in the P-BLTF can be explained by localization of the optical field observed at the air/LT-GaAs interface in between the nanodisks. This indicates that a significant amount

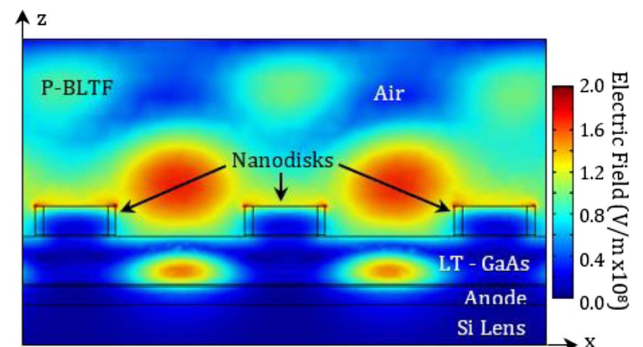


Fig. 9. Electric field distribution at an x - z cross section of the computational domain for the P-BLTF.

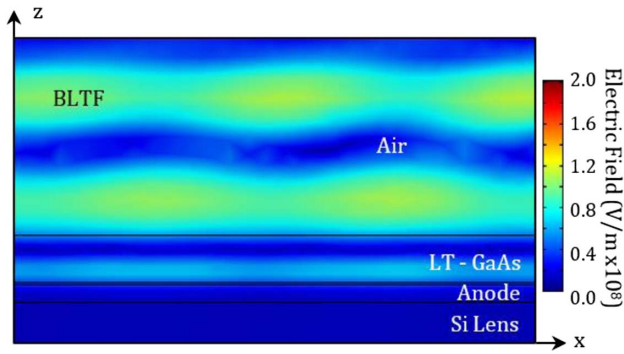


Fig. 10. Electric field distribution at an x - z cross section of the computational domain for the BLTF.

of photocarriers will be generated at the farthest point in the photoconductor from the anode. In contrast, the optical field at the air/LT-GaAs interface in the BLTF design is not as strong, with more of the field focused at the LT-GaAs/anode interface. This indicates that the responsivity of these designs could be tuned by increasing or decreasing the thickness of the LT-GaAs layer.

The final study considered in this work examines the effect of increasing the Schottky–Read–Hall carrier recombination time. Physically, this would represent utilizing higher temperature-grown GaAs photoconductive layer because the growth temperature is the main factor dictating carrier recombination time [50]. The carrier lifetime $\tau_n = \tau_p$ is varied across values of 0.48, 4.8, and 48 ps in Figs. 11 and 12. The anode photocurrent is calculated for each of the four designs, similar to the results shown in Fig. 8. For better comparison, the results are summarized into a peak anode photocurrent and FWHM, as shown in Figs. 11 and 12, respectively.

For all designs, with the exception of the conventional electrode, the peak photocurrent increases slightly with increasing the carrier lifetime. Across the 0.48 to 48 ps range, there is a peak photocurrent increase of 56.8 to 65.1 mA for the P-BLTF, 14.8 to 17.6 mA for the BLTF, 1.7 to 2.0 mA for the nanograting, and a decrease of 0.17 to 0.13 mA for the conventional design. In the first three designs, the full area of the optical

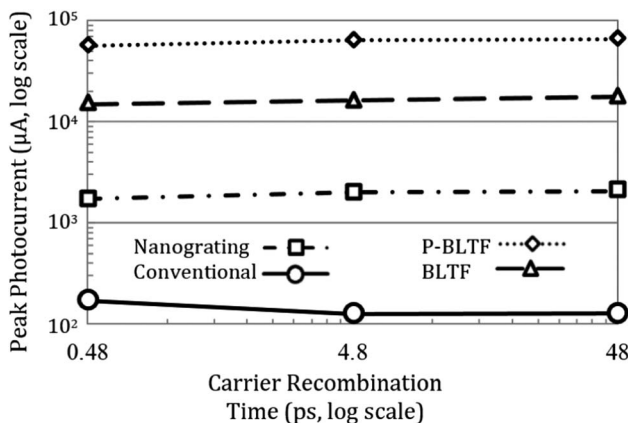


Fig. 11. Peak anode photocurrent of each of the four electrode designs as a function of carrier recombination time $\tau_{n,p}$.

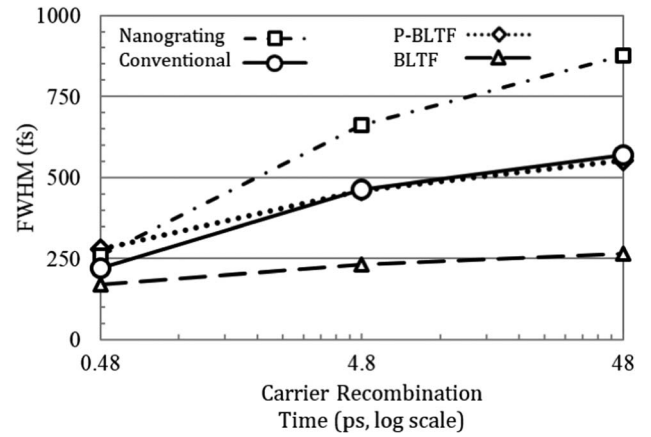


Fig. 12. FWHM of each of the four electrode designs as a function of carrier recombination time $\tau_{n,p}$.

excitation is utilized regardless of carrier recombination time. Although the majority of generated photocarriers are collected before being recombined in the $\tau_{n,p} = 0.48$ ps case, there is still a minority that recombine before reaching the anode. Increasing $\tau_{n,p}$ minimizes this minor recombination, resulting in the slight increase in the observed peak photocurrent.

The FWHM of the anode current is observed in Fig. 12 to increase with carrier recombination time for all designs, from 221 to 569 fs for the P-BLTF, 170 to 264 fs for the BLTF, 280 to 876 fs for the nanograting, and 258 to 552 fs for the conventional. For the conventional anode, the increase in FWHM can be attributed to the increased contribution from the carriers more than 100 nm from the electrode generated at the excitation peak. These carriers take longer to reach the anode and therefore broaden the current pulse. Similarly, in the P-BLTF, there is observed a significant concentration of optical energy at the air/LT-GaAs interface. This region was 120 nm from the anode, and increasing the recombination time increases the total number of carriers generated in the region that are able to reach the anode before recombining. In contrast, the increase in FWHM was lowest for the BLTF. This is due to the fact that the optical energy localized at the air/LT-GaAs interface was less as compared with the P-BLTF design. There is a greater percentage of generated photocarriers near the anode, thereby resulting in a lower FWHM at high carrier recombination times as compared with the P-BLTF. The FWHM is highest and has the most drastic increase with recombination time for the nanograting design. Here, the LT-GaAs layer was 500 nm, over four times the thickness in the P-BLTF and BLTF designs. Although the nanograting design does induce plasmonic localization of the optical field near the anode, much of the photocarriers are generated deeper in the LT-GaAs, thus leading to a broadening of the collected current pulse.

As discussed in Section 2.C, the carrier screening effect has not been taken into account in any of the results here. However, it is possible to estimate the average effect on the optical power transmittance and, consequently, the induced photocurrent [51]. First note that the optical conductivity is proportional to the total free carrier concentration, $N_{\text{tot}} = N_D + N_{\text{opt}}$. Here, N_{opt} is the concentration of optically

Table 5. Summary of the Expected Carrier Screening Effect

Model	σ (S/m)	σ_E (S/m)	R^2	R_E^2	$\frac{1-R^2}{1-R_E^2} - 1$
Conventional	$1.10 \cdot 10^3$	$3.55 \cdot 10^3$	11.3%	14.0%	3.2%
Nanograting		$4.54 \cdot 10^3$		15.0%	4.3%
BLTF		$2.74 \cdot 10^3$		12.1%	1.7%
P-BLTF		$5.83 \cdot 10^3$		16.2%	5.8%

generated carriers. For low incident optical power, $N_{\text{opt}} \ll N_D$ and our approximation of a constant optical conductivity is reasonable. As the incident optical power increases with time, there eventually comes a point when $N_{\text{opt}} \geq N_D$ and the optical conductivity and surface reflectance will increase. To analyze this effect, the spatial and temporal average in N_{tot} is calculated at the Air/LT-GaAs surface and is used to estimate the expected increased optical conductivity σ_E , power reflectance $(R_E)^2$, and expected overestimation in optical power transmittance $(1 - R^2)/(1 - (R_E)^2) - 1$ in the current model. These estimated data are shown in Table 5. Here, R^2 represents the reflectance in the current model (i.e., without the carrier screening effect). Neglecting the carrier screening effect leads to overestimation of the optical power transmittance by $\sim 5.8\%$ for the P-BLTF design. This is due to the large optical fields at the LT-GaAs surface generated by the plasmonic nanostructures. In addition, it is important to note that calculated carrier screening effect is higher in the nanograting design as compared with the conventional one. This is consistent with the validation of our model with experimental data in Fig. 3, where the observed 20% overestimation in the calculated and experimental photocurrent enhancement is consistent with the observed difference in the carrier screening effect of the nanograting and conventional configurations. It is important to note that this simplified model underestimates the reflectance of the BLTF and P-BLTF designs, as can be seen by comparing Table 5 with the reflectance spectra of Fig. 6(b). The simplified model used to calculate the values of Table 5 considers only the change in surface reflection of the air/LT-GaAs interface and does not include the effects of the nanodisk array and bottom electrode.

5. DISCUSSION AND CONCLUSION

The thin-film THz-PCA designs computationally studied in this work demonstrate significant improvement in their optical-to-THz conversion capabilities as compared with previously proposed designs. The P-BLTF design showed the highest peak photocurrent, almost 336 and 32.6 times higher than the conventional and nanograting electrodes, respectively. The BLTF maintained the lowest overall FWHM, almost 265 fs at the longest carrier recombination time of 48 ps. This value for carrier recombination is much longer than that of LT-GaAs. The results demonstrate the BLTF design's capability of maintaining an ultrafast response regardless of carrier recombination time. Removing the requirement of short carrier lifetime has the potential for exploring other photoconductive material systems with higher quantum efficiency, thus providing even further increase in the optically induced THz photocurrent.

High-efficiency, high-power THz-PCA development is an integral step in the movement of THz time-domain imaging

and spectroscopy technology from the research setting into real world applications. The computational model in this work has demonstrated the ability to effectively predict the relative performance of various THz-PCA electrode configurations. This can be a valuable tool for researchers developing high-performance THz-PCAs, as it allows the device performance to be predicted before expensive and time-consuming prototyping and testing. Future work is ongoing to develop the fabrication process required for prototyping of the P-BLTF and BLTF designs, allowing their THz power emission to be experimentally measured and compared with conventional-style THz-PCA emitters.

Funding. National Science Foundation (NSF) (1548550); University of Arkansas College of Engineering Seed Funding Program; University of Arkansas Doctoral Academy Fellowship.

REFERENCES

1. M. Tonouchi, "Cutting-edge terahertz technology," *Nat. Photonics* **1**, 97–105 (2007).
2. D. Saeedkia, *Handbook of Terahertz Technology for Imaging* (Sensing and Communications, 2013).
3. P. U. Jepsen, R. H. Jacobsen, and S. R. Keiding, "Generation and detection of terahertz pulses from biased semiconductor antennas," *J. Opt. Soc. Am. B* **13**, 2424–2436 (1996).
4. D. Grischkowsky, S. Keiding, M. Van Exter, and C. Fattinger, "Far-infrared time-domain spectroscopy with terahertz beams of dielectrics and semiconductors," *J. Opt. Soc. Am. B* **7**, 2006–2015 (1990).
5. N. M. Burford, M. O. El-Shenawee, C. B. O'Neal, and K. J. Olejniczak, "Terahertz imaging for nondestructive evaluation of packaged power electronic devices," *Int. J. Emerg. Technol. Adv. Eng.* **4**, 395–401 (2014).
6. P. Hoyer, G. Matthäus, U. Blumröder, K. Fuchsels, and S. Nolte, "Induced terahertz emission as a probe for semiconductor devices," *Appl. Phys. Lett.* **99**, 221112 (2011).
7. N. Hasegawa, T. Löffler, M. Thomson, and H. G. Roskos, "Remote identification of protrusions and dents on surfaces by terahertz reflectometry with spatial beam filtering and out-of-focus detection," *Appl. Phys. Lett.* **83**, 3996–3998 (2003).
8. L. Minkevičius, R. Suzanovičienė, S. Balakauskas, G. Molis, A. Krotkus, G. Valušis, and V. Tamošiūnas, "Detection of tab wire soldering defects on silicon solar cells using terahertz time-domain spectroscopy," *Electron. Lett.* **48**, 932–934 (2012).
9. M. D. King, W. D. Buchanan, and T. M. Korter, "Understanding the terahertz spectra of crystalline pharmaceuticals: terahertz spectroscopy and solid-state density functional theory study of (S)-(+)-ibuprofen and (RS)-ibuprofen," *J. Pharm. Sci.* **100**, 1116–1129 (2011).
10. A. Grange, "Terahertz spectroscopy: an investigation into the use of terahertz radiation to detect/sense drugs, pharmaceuticals and polymorphs," http://www.engineering.leeds.ac.uk/e-engineering/documents/Grange_for_publication_000.pdf
11. T. C. Bowman, M. El-shenawee, and L. K. Campbell, "Terahertz imaging of excised breast tumor tissue on paraffin sections," *IEEE Trans. Antennas Propag.* **63**, 2088–2097 (2015).

12. A. M. Hassan, D. C. Hufnagle, M. El-shenawee, and G. E. Pacey, "Terahertz imaging for margin assessment of breast cancer tumors," in *Proceedings of IEEE International Microwave Symposium* (IEEE, 2012).
13. P. C. Ashworth, E. Pickwell-MacPherson, E. Provenzano, S. E. Pinder, A. D. Purushotham, M. Pepper, and V. P. Wallace, "Terahertz pulsed spectroscopy of freshly excised human breast cancer," *Opt. Express* **17**, 12444–12454 (2009).
14. C. Yu, S. Fan, Y. Sun, and E. Pickwell-Macpherson, "The potential of terahertz imaging for cancer diagnosis: a review of investigations to date," *Quant. Imaging Med. Surg.* **2**, 33–45 (2012).
15. I. Javaid, "Terahertz time of flight detection for absolute thickness," M. S. thesis, (Optical Science and Engineering University, North Carolina, Charlotte, 2010).
16. H. Nakanishi, K. Takeya, I. Kawayama, H. Murakami, and M. Tonouchi, "Depth measurement of through-silicon via using THz time-domain spectroscopy," in *International Conference on Infrared, Millimeter, Terahertz Waves* (IEEE, 2011).
17. N. Laman and D. Grischkowsky, "Terahertz conductivity of thin metal films," *Appl. Phys. Lett.* **93**, 051105 (2008).
18. N. Matsumoto, T. Hosokura, T. Nagashima, and M. Hangyo, "Measurement of the dielectric constant of thin films by terahertz time-domain spectroscopic ellipsometry," *Opt. Lett.* **36**, 265–267 (2011).
19. D. Hashimshony, I. Geltner, G. Cohen, Y. Avitzour, A. Zigler, and C. Smith, "Characterization of the electrical properties and thickness of thin epitaxial semiconductor layers by THz reflection spectroscopy," *J. Appl. Phys.* **90**, 5778–5781 (2001).
20. J. F. Federici, B. Schulkin, F. Huang, D. Gary, R. Barat, F. Oliveira, and D. Zimdars, "THz imaging and sensing for security applications—explosives, weapons and drugs," *Semicond. Sci. Technol.* **20**, S266–S280 (2005).
21. M. C. Kemp, P. F. Taday, B. E. Cole, J. A. Cluff, A. J. Fitzgerald, and W. R. Tribe, "Security applications of terahertz technology," *Proc. SPIE* **5070**, 44–52 (2003).
22. L. Ho, M. Pepper, and P. Taday, "Terahertz spectroscopy: signatures and fingerprints," *Nat. Photonics* **2**, 541–543 (2008).
23. H.-B. Liu, H. Zhong, N. Karpowicz, Y. Chen, and X.-C. Zhang, "Terahertz spectroscopy and imaging for defense and security applications," *Proc. IEEE* **95**, 1514–1527 (2007).
24. S. G. Park, K. H. Jin, M. Yi, J. C. Ye, J. Ahn, and K. H. Jeong, "Enhancement of terahertz pulse emission by optical nanoantenna," *ACS Nano* **6**, 2026–2031 (2012).
25. A. Jooshesh, L. Smith, M. Masnadi-shirazi, V. Bahrami-yekta, T. Tiedje, T. E. Darcie, and R. Gordon, "Nanoplasmonics enhanced terahertz sources," *Opt. Express* **22**, 27992–28001 (2014).
26. C. W. Berry, N. Wang, M. R. Hashemi, M. Unlu, and M. Jarrahi, "Significant performance enhancement in photoconductive terahertz optoelectronics by incorporating plasmonic contact electrodes," *Nat. Commun.* **4**, 1622 (2013).
27. C. W. Berry, M. R. Hashemi, and M. Jarrahi, "Generation of high power pulsed terahertz radiation using a plasmonic photoconductive emitter array with logarithmic spiral antennas," *Appl. Phys. Lett.* **104**, 081122 (2014).
28. C. W. Berry and M. Jarrahi, "Terahertz generation using plasmonic photoconductive gratings," *New J. Phys.* **14**, 105029 (2012).
29. S. Yang, M. R. Hashemi, C. W. Berry, and M. Jarrahi, "7.5% optical-to-terahertz conversion efficiency offered by photoconductive emitters with three-dimensional plasmonic contact electrodes," *IEEE Trans. Terahertz Sci. Technol.* **4**, 1–7 (2014).
30. N. T. Yardimci, S. Yang, C. W. Berry, and M. Jarrahi, "High-power terahertz generation using large-area plasmonic photoconductive emitters," *IEEE Trans. Terahertz Sci. Technol.* **5**, 223–229 (2015).
31. N. Khiabani, Y. Huang, Y. Shen, S. Boyes, and Q. Xu, "A novel simulation method for THz photoconductive antenna characterization," in *EUCAP* (IEEE, 2013), pp. 751–754.
32. N. Khiabani, Y. Huang, Y. C. Shen, and S. J. Boyes, "Theoretical modeling of a photoconductive antenna in a terahertz pulsed system," *IEEE Trans. Antennas Propag.* **61**, 1538–1546 (2013).
33. E. Moreno, M. F. Pantoja, and S. G. Garc. "On the simulation of carrier dynamics in terahertz photoconductive antennas," in *EUCAP* (IEEE, 2013), pp. 740–741.
34. E. Moreno, M. F. Pantoja, S. G. Garcia, A. R. Bretones, and R. G. Martin, "Time-domain numerical modeling of THz photoconductive antennas," *IEEE Trans. Terahertz Sci. Technol.* **4**, 490–500 (2014).
35. E. Moreno, M. F. Pantoja, F. G. Ruiz, J. B. Roldán, and S. G. García, "On the numerical modeling of terahertz photoconductive antennas," *J. Infrared, Millimeter, Terahertz Waves* **35**, 432–444 (2014).
36. J. J. Schermer, G. J. Bauhuis, P. Mulder, E. J. Haverkamp, J. van Deelen, A. T. J. van Niftrik, and P. K. Larsen, "Photon confinement in high-efficiency, thin-film III-V solar cells obtained by epitaxial lift-off," in *Proceedings of Symposium F on Thin Film and Nanostructured Materials for Photovoltaics* (EMRS, 2006), pp. 645–653.
37. G. J. Bauhuis, P. Mulder, E. J. Haverkamp, J. Huijben, and J. J. Schermer, "26.1% thin-film GaAs solar cell using epitaxial lift-off," *Sol. Energy Mater. Sol. Cells* **93**, 1488–1491 (2009).
38. N. Burford and M. El-Shenawee, "Plasmonic enhancement of irregular shape nano-patch for thin film silicon solar cells," *Appl. Comput. Electromagn. Soc. J.* **28**, 359–373 (2013).
39. N. Burford and M. El-Shenawee, "Optimization of silver nanotoroid arrays for the absorption enhancement of silicon thin-film solar cells," *Plasmonics* **10**, 225–232 (2015).
40. P. Demeester, I. Pollentier, P. De Dobbelaere, C. Brys, and P. Van Daele, "Epitaxial lift-off and its applications," *Semiconductor Sci. Tech.* **8**, 1124–1135 (1993).
41. S. E. Ralph and D. Grischkowsky, "Trap-enhanced fields in semi-insulators: The role of electrical and optical carrier injection," *Appl. Phys. Lett.* **59**, 1972–1974 (1991).
42. J. Hoffmann, C. Hafner, P. Leidenberger, J. Hesselbarth, and S. Burger, "Comparison of electromagnetic field solvers for the 3D analysis of plasmonic nano antennas," *Proc. SPIE* **7390**, 73900J (2009).
43. S. L. Chuang, *Physics of Photonic Devices* (Wiley, 2009).
44. M. Sotoodeh, A. H. Khalid, and A. A. Rezaazadeh, "Empirical low-field mobility model for III-V compounds applicable in device simulation codes," *J. Appl. Phys.* **87**, 2890–2900 (2000).
45. S. Selberherr, W. Hansch, M. Seavey, and J. Slotboom, "The evolution of the MINIMOS mobility model," *Solid-State Electron.* **33**, 1425–1436 (1990).
46. K. Moon, I.-M. Lee, J.-H. Shin, E. S. Lee, N. Kim, W.-H. Lee, H. Ko, S.-P. Han, and K. H. Park, "Bias field tailored plasmonic nano-electrode for high-power terahertz photonic devices," *Sci. Rep.* **5**, 13817 (2015).
47. D. E. Aspnes and A. A. Studna, "Dielectric functions and optical parameters of Si, Ge, GaP, GaAs, GaSb, InP, InAs, and InSb from 1.5 to 6.0 eV," *Phys. Rev. B* **27**, 985–1009 (1983).
48. P. Johnson and R. Christy, "Optical constants of transition metals: Ti, V, Cr, Mn, Fe, Co, Ni, and Pd," *Phys. Rev. B* **9**, 5056–5070 (1974).
49. A. D. Rakic, A. B. Djurišić, J. M. Elazar, and M. L. Majewski, "Optical properties of metallic films for vertical-cavity optoelectronic devices," *Appl. Opt.* **37**, 5271–5283 (1998).
50. E. S. Harmon, D. D. Nolte, N. Otsuka, and C. L. Chang, "Carrier lifetime versus anneal in low temperature growth GaAs," *Appl. Phys. Lett.* **63**, 2248–2250 (1993).
51. K. Tsen, *Ultrafast Dynamical Processes in Semiconductors* (Springer, 2004).